PCCP

PAPER

View Article Online
View Journal | View Issue

Cite this: *Phys. Chem. Chem. Phys.*, 2023, **25**, 17840

Rate constant and branching ratio of the reaction of ethyl peroxy radicals with methyl peroxy radicals

Cuihong Zhang,[abc] Chuanliang Li,[cd] Weijun Zhang,[a] Xiaofeng Tang,[a] Laure Pillier,[c] Coralie Schoemaecker[c] and Christa Fittschen *[c]

Received 13th March 2023,
Accepted 22nd June 2023

DOI: 10.1039/d3cp01141k

rsc.li/pccp

The cross-reaction of ethyl peroxy radicals ($C_2H_5O_2$) with methyl peroxy radicals (CH_3O_2) (R1) has been studied using laser photolysis coupled to time resolved detection of the two different peroxy radicals by continuous wave cavity ring down spectroscopy (cw-CRDS) in their AÃ–X̃ electronic transition in the near-infrared region, $C_2H_5O_2$ at 7602.25 cm^{-1}, and CH_3O_2 at 7488.13 cm^{-1}. This detection scheme is not completely selective for both radicals, but it is demonstrated that it has great advantages compared to the widely used, but unselective UV absorption spectroscopy. Peroxy radicals were generated from the reaction of Cl-atoms with the appropriate hydrocarbon (CH_4 and C_2H_6) in the presence of O_2, whereby Cl-atoms were generated by 351 nm photolysis of Cl_2. For different reasons detailed in the manuscript, all experiments were carried out under excess of $C_2H_5O_2$ over CH_3O_2. The experimental results were best reproduced by an appropriate chemical model with a rate constant for the cross-reaction of $k = (3.8 \pm 1.0) \times 10^{-13}$ cm^3 s^{-1} and a yield for the radical channel, leading to CH_3O and C_2H_5O, of ($\phi_{1a} = 0.40 \pm 0.20$).

Introduction

The oxidation of volatile organic compounds (VOCs) in the troposphere is mainly driven by hydroxyl radicals (OH) and leads, after addition of O_2, to the formation of organic peroxy radicals (RO_2). The fate of these RO_2 radicals depends on the chemical composition of the environment and a detailed review on their chemistry has been given by G. Tyndall and collegues.[1,2] Briefly, in a polluted atmosphere they mainly react with nitric oxide (NO) to form alkoxy radicals or react with nitrogen dioxide (NO_2) to form peroxynitrates (RO_2NO_2). Subsequent to the reaction with NO, alkoxy radicals can react with O_2 to form hydroperoxy radicals (HO_2) together with carbonyl compounds. HO_2 further oxidises NO into NO_2 and thus regenerates OH, closing the quasi-catalytic cycle. The photolysis of the produced NO_2 leads subsequently to the formation of ozone (O_3) and is the only relevant formation path of tropospheric ozone. In clean environments with low NO_x (NO_x = NO + NO_2) concentrations, the fate of RO_2 change and their dominant loss becomes the reaction with HO_2 forming hydroperoxides ROOH and terminating the radical reaction chain. Other reaction pathways under low NO_x conditions for RO_2 radicals are either self-reaction ($RO_2 + RO_2$) or cross-reaction with other RO_2 ($RO_2 + R'O_2$)[1] or with OH radicals ($RO_2 + OH$).[3]

Methane and ethane are amongst the most abundant hydrocarbons, and their atmospheric oxidation leads to the formation of methyl peroxy (CH_3O_2) and ethyl peroxy ($C_2H_5O_2$) radicals. For both radicals, the kinetic and product distribution for the self-reaction has been studied numerous times (for CH_3O_2[4–12] and for $C_2H_5O_2$[13–26]), the same is true for their reaction with HO_2 (for CH_3O_2[5,9,27–32] and for $C_2H_5O_2$[13,14,20,26,30,33–35]). Their reaction with OH radicals has been the subject of a few studies (for CH_3O_2[3,36–41] and for $C_2H_5O_2$[42–44]). The cross-reaction between both peroxy radicals has only been measured once using UV absorption spectroscopy[45] whereby the experimental details given in that paper are sparse and it is not clear how the rate constant was extracted from the absorption time profiles measured at only one wavelength where the cross sections of both radicals are very similar. As for the product distribution of this cross reaction, three pathways can be expected:

$$C_2H_5O_2 + CH_3O_2 \rightarrow C_2H_5O + CH_3O + O_2 \quad (R1a)$$

[a] *Anhui Institute of Optics and Fine Mechanics, Hefei Institutes of Physical Science, Chinese Academy of Sciences, Hefei 230031, Anhui, China*
[b] *Science Island Branch, Graduate School, University of Science and Technology of China, Hefei 230026, Anhui, China*
[c] *Université Lille, CNRS, UMR 8522-PC2A-Physicochimie des Processus de Combustion et de l'Atmosphère, F-59000 Lille, France. E-mail: christa.fittschen@univ-lille.fr*
[d] *Shanxi Engineering Research Center of Precision Measurement and Online Detection Equipment and School of Applied Science, Taiyuan University of Science and Technology, Taiyuan 030024, China*

$$\rightarrow C_2H_5OH/CH_3OH + CH_2O/CH_3CHO + O_2 \quad (R1b)$$

$$\rightarrow C_2H_5O_2CH_3 + O_2 \quad (R1c)$$

whereby currently no information is available on the branching ratio between these pathways.

The investigation of this reaction is not straightforward, because secondary chemistry cannot be avoided. Both radicals will react in self-reactions, leading to analogous reaction products. The measurements are complicated, because the product of the reaction path (R1a) leads, after rapid reaction with O_2, to the formation of HO_2 radicals

$$CH_3O + O_2 \rightarrow CH_2O + HO_2 \quad (R2)$$

$$C_2H_5O + O_2 \rightarrow CH_3CHO + HO_2 \quad (R3)$$

with the HO_2 radicals reacting subsequently with both peroxy radicals:

$$CH_3O_2 + HO_2 \rightarrow CH_3O_2H + O_2 \quad (R4)$$

$$C_2H_5O_2 + HO_2 \rightarrow C_2H_5O_2H + O_2 \quad (R5)$$

The rate constants of (R4) and (R5) are faster than the rate constant of (R1), and thus the CH_3O_2 and $C_2H_5O_2$ decays are accelerated. Therefore, determining the rate constant k_1 from observed CH_3O_2 and $C_2H_5O_2$ decays depends also on the branching ratio k_{1a}/k_1 as well as the branching ratios for the two self-reactions used in the data treatment: for a given experimental $C_2H_5O_2$ or CH_3O_2 decay the retrieved rate constant k_1 will decrease with increasing branching ratio.

In this work we present a more direct measurement of the rate constant of (R1). Measurements have been carried out under an excess of $C_2H_5O_2$ radicals over CH_3O_2, and both radicals have been followed in their $\tilde{A}$–$\tilde{X}$ electronic transition using two different wavelengths. HO_2 concentration time profiles have been measured simultaneously in a highly selective way in the $2\nu_1$ vibrational overtone at 6638.21 cm^{-1}.

Experimental

Experimental setup

The setup has been described in detail before[46–49] and is only briefly discussed here. The setup mainly consists of a 0.79 m long flow reactor made of stainless steel. The beam of a pulsed excimer laser (Lambda Physik LPX 202i), running at 351 nm, passed the reactor longitudinally. The flow reactor contained two identical continuous wave cavity ring-down spectroscopy (cw-CRDS) absorption paths, which were installed in a small angle with respect to the photolysis path. An overlap of the near IR-path with the photolysis beam of 0.288 m is achieved with an excimer beam width delimited to 2 cm. Both beam paths were tested for a uniform overlap with the photolysis beam before experiments. For this purpose, both cw-CRDS instruments were operated to simultaneously measure HO_2 concentrations. Deviations between HO_2 concentrations were less than 5%, demonstrating that the photolysis laser was well aligned, *i.e.* both light paths probed a very similar photolysed volume in the reactor. A small helium purge flow prevented the mirrors from being contaminated. Three different DFB lasers are used for the detection of the three species: HO_2: NEL NLK1E5GAAA, 6629 ± 17 cm^{-1}, on CRDS path 1, CH_3O_2: NEL NLK1B5EAAA, 7480 ± 20 cm^{-1} on CRDS path 2, $C_2H_5O_2$: AOI-1312-BF-20-CW-F1-H2-N127, 7622 ± 15 cm^{-1} on CRDS path 2. They are coupled into one of the cavities by systems of lenses and mirrors. Each probe beam passed an acousto-optic modulator (AOM, AAoptoelectronic) to rapidly turn off the 1st order beam once a threshold for light intensity at the exit of the cavity was reached, in order to measure the ring-down event. Then, the decay of light intensity was recorded and an exponential fit is applied to retrieve the ring-down time. The absorption coefficient α is derived from eqn (1).

$$\alpha = [A] \times \sigma_A = \frac{R_L}{c}\left(\frac{1}{\tau} - \frac{1}{\tau_0}\right) \quad (1)$$

where τ is the ring-down time with an absorber present (*i.e.* after the photolysis pulse); τ_0 is the ring-down time with no absorber present (*i.e.* before the photolysis pulse); σ_A is the absorption cross section of the absorbing species A; R_L is the ratio between cavity length (79 cm) and effective absorption path (28.8 cm); c is the speed of light.

Ethyl- and methylperoxy radicals were generated by pulsed 351 nm photolysis of $C_2H_6/CH_4/Cl_2/O_2$ mixtures inducing the following reactions:

$$Cl_2 + h\nu_{351\,nm} \rightarrow 2\ Cl \quad (R7)$$

$$CH_4 + Cl \rightarrow CH_3 + HCl \quad (R8)$$

$$C_2H_6 + Cl \rightarrow C_2H_5 + HCl \quad (R9)$$

$$CH_3 + O_2\ (+\ M) \rightarrow CH_3O_2\ (+\ M) \quad (R10)$$

$$C_2H_5 + O_2\ (+\ M) \rightarrow C_2H_5O_2\ (+\ M) \quad (R11a)$$

$$C_2H_5 + O_2 \rightarrow C_2H_4 + HO_2 \quad (R11b)$$

In order to rapidly convert the different radicals (C_2H_5, CH_3, C_2H_5O and CH_3O) into peroxy or HO_2 radicals ((R2), (R3), (R10) and (R11)), all experiments have been carried out in 100 Torr O_2 (Air Liquide, Alpha Gaz 2).

C_2H_6 (Air Liquide, N35), CH_4 (Air Liquide, N45) and Cl_2 (Air Liquide, 5% in Helium) were used directly from the cylinder: a small flow was added to the mixture through a calibrated flow meter (Bronkhorst, Tylan). All experiments were carried out at 298 K.

Results and discussion

Determination of the absorption cross sections

Detecting peroxy radicals in the $\tilde{A}$–$\tilde{X}$ electronic transition in the near IR region has the potential of a more selective detection for peroxy radicals compared to UV absorption spectroscopy. In order to demonstrate this, we have carried out measurements for the determination of the rate constant of the cross reaction between CH_3O_2 and $C_2H_5O_2$ radicals. The rate constant of this reaction was measured only once using UV absorption

spectroscopy[45] whereby the experimental details given in that paper were sparse. It is not clear how the rate constant was extracted from the absorption time profiles measured only at one wavelength where the cross sections of both radicals are very similar.

The Ã–X̃ transitions of peroxy radicals consist generally of peaks with a few cm^{-1} FWHM on a rather broad background.[50] To check for the mutual selectivity of the detection for both radicals, the absorption cross sections for both radicals have been measured at three different wavelengths: at one "peak" of the Ã–X̃ transitions of the CH_3O_2 radical at 7488.14 cm^{-1} (named in the following M1, green symbols in Fig. 1), at the maximum of the transition of $C_2H_5O_2$ at 7596.47 cm^{-1} (named E1, red symbols in Fig. 1) and at a "plateau" at 7602.25 cm^{-1} (named E2, blue symbols in Fig. 1).

The upper graphs of Fig. 1 show for one Cl-concentration the absorption time profiles for both radicals (left: CH_3O_2, right: $C_2H_5O_2$) at all three wavelengths. It can be seen that both radicals still absorb at the wavelength corresponding to the transition of the counterpart radical: for both radicals the absorption at its peak is around 4 times larger than at the peak of the counterpart radical (second column Table 1). The absorption cross sections at the peak wavelengths are known from earlier works[3,51,52] and have been used here to obtain the absorption cross sections at the peak wavelength of the counterpart radical from the relative intensities in Fig. 1 type experiments (experiments using 3 different Cl-atom concentrations have been carried out). The results are summarized in Table 1 and illustrated in the lower graph of Fig. 1.

Table 1 Ratio and absorption cross sections for CH_3O_2, $C_2H_5O_2$ and CH_4 at three wavelengths

	Ratio ($\sigma_{peak}/\sigma_{off}$)	σ (M1)/cm^2 7488.13 cm^{-1}	σ (E1)/cm^2 7596.47 cm^{-1}	σ (E2)/cm^2 7602.25 cm^{-1}
CH_3O_2	4.0	2.2×10^{-20}	*5.5×10^{-21}*	*5.5×10^{-21}*
$C_2H_5O_2$	6.6/5.0	*1.5×10^{-21}*	1.0×10^{-20}	7.6×10^{-21}
CH_4[53]		1.2×10^{-24}	1.1×10^{-23}	5.0×10^{-25}
Ratio $\frac{\sigma(CH_3O_2)}{\sigma(C_2H_5O_2)}$		14.6	0.55 (= 1/1.81)	0.72 (= 1/1.38)

It can be seen that the absorption cross sections for both radicals at the "counterpart wavelengths" (in *italic* in Table 1) are small (1.5 and 5.5 $\times$ 10^{-21} cm^{-2}), but not zero, and thus complete selectivity cannot be obtained.

Determination of the rate constant

To get best selectivity for investigating the cross reaction between both radicals, $C_2H_5O_2$ was used for all experiments in excess over CH_3O_2 for different reasons:

• To limit the reaction of Cl-atoms with peroxy radicals: the reaction of Cl-atoms with CH_4 is much slower than the reaction of Cl-atoms with C_2H_6 (0.01 and 5.9 $\times$ 10^{-11} cm^3 s^{-1} for CH_4 and C_2H_6, respectively).[54] Therefore, to even obtain identical

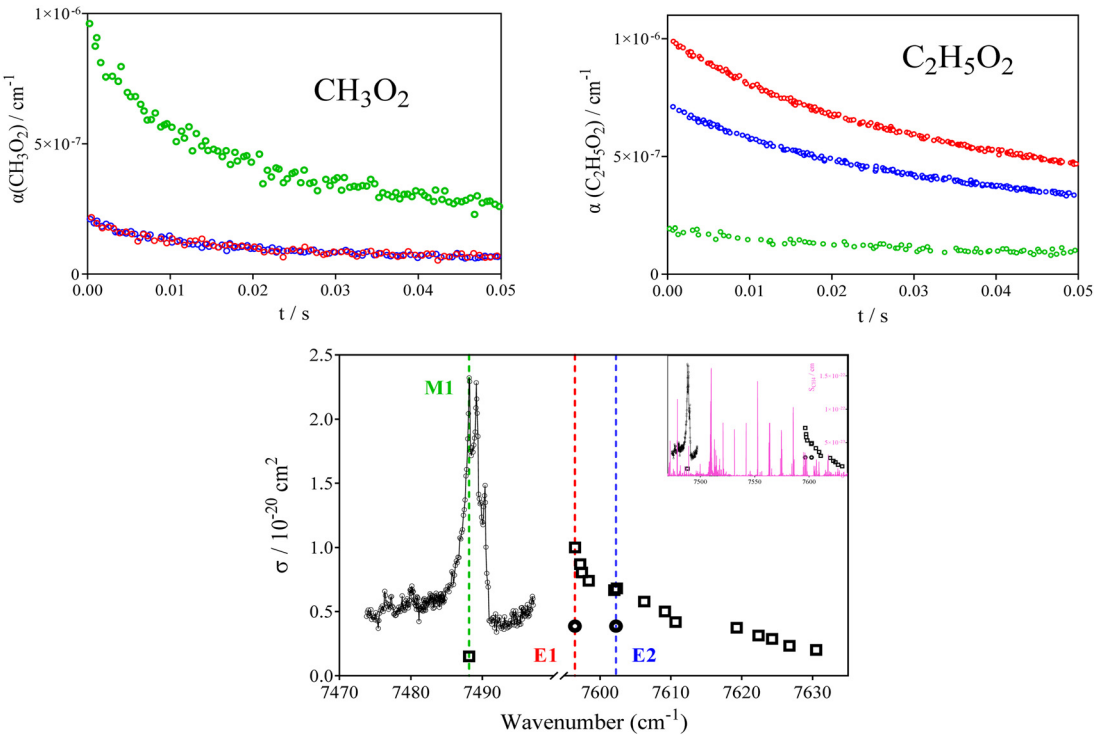

Fig. 1 CH_3O_2 (upper left graph, $[Cl]_0$ = 4.2 $\times$ 10^{13} cm^{-3}, $[CH_4]$ = 1.9 $\times$ 10^{17} cm^{-3}) and $C_2H_5O_2$ (upper right graph: $[Cl]_0$ = 1.0 $\times$ 10^{14} cm^{-3}, $[C_2H_6]$ = 4.4 $\times$ 10^{16} cm^{-3}) profiles obtained at the three different wavelengths represented by colored vertical lines in the lower graph. Lower graph shows spectrum for both species (CH_3O_2 as circles, adapted from Farago *et al.*[51] and $C_2H_5O_2$ as square adapted from Zhang *et al.*[52]), main graph shows zoom on both sections with *x*-axis interrupted, insert shows continuous wavelength scale. Magenta lines in insert represent CH_4 spectrum from HITRAN database.[53]

CH_3O_2 and $C_2H_5O_2$ concentrations, already 580 times more CH_4 than C_2H_6 is needed. And because CH_4 is absorbing in the near IR region (the absorption cross sections for CH_4 at the three wavelengths are given in Table 1 and is shown as magenta stick spectrum[53] in Fig. 1), the amount of CH_4 that can be added in our experiments is limited to a few 10^{17} cm^{-3}. If an excess of CH_3O_2 would have been chosen, only a few 10^{13} cm^{-3} C_2H_6 would need to be added to obtain comparable $C_2H_5O_2$ concentrations. Such low hydrocarbon concentrations would lead to Cl-atom decays too slow to avoid major complications due to the reaction of Cl-atoms with CH_3O_2 or $C_2H_5O_2$.

• To limit absorption of the ''counterpart'' radical and thus increase selectivity: the ratio of the absorption cross sections between both radicals at a given wavelength (last row of Table 1) is higher at the methyl peroxy transition: $\sigma(CH_3O_2)$ is 14.6 times higher compared to $\sigma(C_2H_5O_2)$ at (M1), while the inverse ratio is only 1.81 and 1.38 at (E1) and (E2), respectively. Therefore, in the example of a 10-fold (5-fold) excess of CH_3O_2 over $C_2H_5O_2$, the absorbance at (M1) would be more than 99% (98%) due to CH_3O_2 (*i.e.* excellent selectivity), but at (E1) only 15% (27%) and at (E2) only 12% (22%) of the absorbance would be due to $C_2H_5O_2$, respectively. In the example of a 10-fold (5-fold) excess of $C_2H_5O_2$ over CH_3O_2, the absorbance at (E1) would be around 95% (90%) and at (E2) 93% (87%) due to $C_2H_5O_2$ (*i.e.* still good selectivity), but now at (M1) around 59% (75%) of the signal is due to CH_3O_2 absorption.

• To maximize the importance of the cross-reaction: the self-reaction of $C_2H_5O_2$ is 3.5 times slower than that of CH_3O_2 (or 2 times, taking the very recent determination of the CH_3O_2 self-reaction rate constant by Onel *et al.*[12]), making the loss through self-reaction less important in a reaction system with excess $C_2H_5O_2$ compared to excess CH_3O_2.

Therefore, experiments with a 5- to 10-fold excess of $C_2H_5O_2$ over CH_3O_2 should lead to a good sensitivity towards the rate constant of the cross-reaction: decays at (E1) or (E2) represent nearly pure $C_2H_5O_2$ decays mostly governed by the self-reaction, the correction of these profiles due to CH_3O_2 absorption is very minor. Simultaneously measured profiles obtained at (M1) can now be corrected for $C_2H_5O_2$ absorption, and the remaining CH_3O_2 decay is mostly due to the cross reaction with $C_2H_5O_2$: the rate constant of the cross reaction can be extracted with good sensitivity.

Even though the absorption cross section for $C_2H_5O_2$ is higher on (E1) compared to (E2), all experiments have been carried out at (M1) and (E2) due to the much lower CH_4 absorption cross sections at (E2) compared to (E1): even though $C_2H_5O_2$ is used in excess, high CH_4 concentrations (up to 3×10^{17} cm^{-3}) were still added and absorbed too much light at (E1).

Three series of experiments have been carried out, and the experimental conditions are summarized in Table 2. The initial Cl-atom concentrations (column 1) have been measured before each experiment through measuring and fitting HO_2 decays from the reaction of Cl-atoms with excess CH_3OH. C_2H_6 and CH_4 concentrations (column 2 and 3) have been obtained from flow and pressure measurements, and the initial peroxy radical concentrations (column 4 and 5) and their ratio (column 6) have then been calculated using the literature values of the rate constants for (R8) and (R9), as given in Table 3. To demonstrate the relatively good selectivity towards both radicals, the percentage of the absorbances at M1 and E2, that are due to the searched-after radical, have then been calculated using the radical concentrations and the absorption cross sections from Table 1 (column 7 and 8).

Fig. 2 shows the experimental absorption time-profiles obtained at M1 and E2 for the 3 series (highest $C_2H_5O_2$ excess upper graph, note the different *y*-axis for both wavelengths, and lowest $C_2H_5O_2$ excess bottom graphs) as colored dots: the absorption time-profiles obtained at M1, the wavelength mostly selective to CH_3O_2, are shown in the left column, the profiles obtained at E2, mostly selective to $C_2H_5O_2$, are shown in the right column.

The profiles at both wavelengths have been simulated simultaneously using the model from Table 3, by best reproducing the signals at M1 as

$$\alpha_{M1} = \sigma_{CH_3O_2,M_1} \times [CH_3O_2] + \sigma_{C_2H_5O_2,M_1} \times [C_2H_5O_2] \quad (2)$$

and the signals at E2 as:

$$\alpha_{E2} = \sigma_{CH_3O_2,E2} \times [CH_3O_2] + \sigma_{C_2H_5O_2,E2} \times [C_2H_5O_2] \quad (3)$$

using the corresponding absorption cross sections such as given in Table 1. These simulations are shown as full lines. The dotted lines in each graph represent the part of the absorption that is due to the ''major'' radical, *i.e.* CH_3O_2 in the left column and $C_2H_5O_2$ in the right column.

The model contains, next to peroxy self-and cross reactions, also some secondary chemistry of Cl-atoms: these reactions

Table 2 Experimental conditions used for measuring the rate constant of the cross reaction between CH_3O_2 and $C_2H_5O_2$

$[Cl]/10^{13}$ cm^{-3}	$[C_2H_6]/10^{15}$ cm^{-3}	$[CH_4]/10^{17}$ cm^{-3}	$[C_2H_5O_2]_0/10^{13}$ cm^{-3}	$[CH_3O_2]_0/10^{13}$ cm^{-3}	$[C_2H_5O_2]_0/[CH_3O_2]_0$	$\alpha_{C_2H_5O_2}$ at E2 (%)	$\alpha_{CH_3O_2}$ at M1 (%)
8.1	2.90	2.00	7.25	0.85	8.56	92.2	63.2
11.0			9.85	1.15			
13.8			12.4	1.44			
7.4	2.08	2.98	5.95	1.45	4.12	85.1	78.1
10.4			8.37	2.03			
12.5			10.1	2.44			
7.1	1.25	2.98	5.05	2.05	2.46	77.3	85.6
9.2			6.54	2.66			
11.8			8.39	3.41			

Table 3 Reaction mechanism used to fit all experiments in this work

	Reaction	k cm^3 s^{-1}	Ref.
Initiation reactions			
8	$Cl + CH_4 \rightarrow CH_3 + HCl$	1.0×10^{-13}	54
9	$Cl + C_2H_6 \rightarrow C_2H_5 + HCl$	5.9×10^{-11}	54
10	$CH_3 + O_2 + M \rightarrow CH_3O_2 + M$	1.4×10^{-13}	55
11a	$C_2H_5 + O_2 + M \rightarrow C_2H_5O_2 + M$	4.8×10^{-12}	56
11b	$C_2H_5 + O_2 \rightarrow C_2H_4 + HO_2$	3.5×10^{-14}	This work
Peroxy radical self- and cross-reactions			
1a	$C_2H_5O_2 + CH_3O_2 \rightarrow C_2H_5O + CH_3O + O_2$	1.5×10^{-13}	This work
1b	$C_2H_5O_2 + CH_3O_2 \rightarrow$ stable products	2.3×10^{-13}	This work
2	$CH_3O + O_2 \rightarrow CH_2O + HO_2$	1.92×10^{-15}	54
3	$C_2H_5O + O_2 \rightarrow CH_3CHO + HO_2$	8×10^{-15}	57
4	$CH_3O_2 + HO_2 \rightarrow CH_3OOH + O_2$	5.2×10^{-12}	52
5	$C_2H_5O_2 + HO_2 \rightarrow C_2H_5OOH + O_2$	6.2×10^{-12}	52
12a	$2\ C_2H_5O_2 \rightarrow 2\ C_2H_5O + O_2$	3.2×10^{-14}	24
12b	$2\ C_2H_5O_2 \rightarrow$ stable products	7.0×10^{-14}	24
13a	$2\ CH_3O_2 \rightarrow 2\ CH_3O + O_2$	1.3×10^{-13}	54
13b	$2\ CH_3O_2 \rightarrow$ stable products	2.2×10^{-13}	54
14	$CH_3O + HO_2 \rightarrow$ products	1.1×10^{-10}	58
15	$2\ HO_2 \rightarrow H_2O_2 + O_2$	1.7×10^{-12}	59
Secondary Cl-atom reactions			
6a	$Cl + C_2H_5O_2 \rightarrow ClO + C_2H_5O$	$5–8 \times 10^{-11}$	See text
6b	$Cl + C_2H_5O_2 \rightarrow$ Products	$5–8 \times 10^{-11}$	See text
16	$Cl + CH_3O_2 \rightarrow ClO + CH_3O$	7.5×10^{-11}	60
17	$Cl + CH_3O_2 \rightarrow$ Products	7.5×10^{-11}	60
18	$Cl + CH_2O + O_2 \rightarrow HCl + HO_2 + CO$	7.32×10^{-11}	61
19	$C_2H_5O_2/CH_3O_2 + ClO \rightarrow C_2H_5O/CH_3O + ClOO$	1.6×10^{-12}	54
20	$HO_2 + ClO \rightarrow O_2 + HOCl$	6.9×10^{-12}	62
21	$ClOO\ (+ M) \rightarrow Cl + O_2\ (+ M)$	6.2×10^{-13}	62
22	$Cl + O_2\ (+ M) \rightarrow ClO_2\ (+ M)$	1.6×10^{-33}	62
Other secondary chemistry			
23	$C_2H_5O + C_2H_5O_2 \rightarrow$ products	7×10^{-12}	This work
24	$C_2H_5O + HO_2 \rightarrow$ products	1×10^{-10}	63
25	$C_2H_5O_2/CH_3O_2 \rightarrow$ diffusion	2 s^{-1}	This work
26	$HO_2 \rightarrow$ diffusion	3 s^{-1}	This work

could not completely be avoided, even though their impact is minor. Preliminary results in our laboratory indicate that the reaction of Cl-atoms with $C_2H_5O_2$ leads with a rate constant of around 1×10^{-10} cm^3 s^{-1} and a yield of 50% to formation of C_2H_5O and ClO, while no clear statement can currently be made for the fate of the other 50%. The rate constant of this reaction has also been determined by Maricq *et al.*[64] to be 1.6×10^{-10} cm^3 s^{-1}, and therefore this reaction has been included into the mechanism (see Table 3) and tests have been run with the rate constant being varied between 1.0–1.6 $\times$ 10^{-10} cm^3 s^{-1}, but the impact on simulated profiles and thus on the sought-after rate constant was within the noise of the experimental profiles.

Fig. 3 shows for the example of the highest $C_2H_5O_2$ excess (upper graphs of Fig. 2) the breakdown of the fate of the 2 peroxy radicals into the different possible reaction paths: the left graphs represent CH_3O_2, the right graphs $C_2H_5O_2$. The red symbols represent the fraction of the peroxy radical, which has reacted in the cross reaction (R1): it can be seen that for CH_3O_2, this reaction is the major fate for all initial radical concentrations (upper graph represent blue symbols from Fig. 2, lower graph represent green symbols from Fig. 2), while for $C_2H_5O_2$ this reaction is a minor loss. The major reaction path for $C_2H_5O_2$ is its self-reaction (black symbols), with the cross-reaction with HO_2 being the secondary contributor (blue symbols). These two pathways are very minor for CH_3O_2. For both radicals, the fraction having reacted with Cl-atoms (green symbols), is small, up to 5% for CH_3O_2 in the worst case of high initial radical concentration.

Determination of branching ratio

Simultaneously measured HO_2 profiles allow in principle the estimation of the branching ratio for the radical and molecular path of the cross reaction. The right graph of Fig. 4 shows the HO_2 profiles obtained for the series with the highest $C_2H_5O_2$/CH_3O_2 ratio. The initial fast rise of HO_2 has two origins: it is partially due to the reaction of Cl-atoms with the peroxy radicals (R6) and partially due to the small fraction of C_2H_5 radicals that form HO_2 in reaction with O_2 (R11b) rather than the $C_2H_5O_2$ radical. The first process is taken into account in the chemical model by adding a simplified reaction schema (see Table 3), the second process has been implemented to best represent the initial HO_2 concentration and represents less than 1% of the initial C_2H_5 concentration. This observation is in excellent agreement with earlier works.[24,52,65,66] These two processes are finished within a few hundred μs, and the branching ratio of the cross reaction then influences the HO_2 concentration at longer reaction time. This is conceivable, because the HO_2 concentration at longer reaction times represents the steady-state concentration between production from

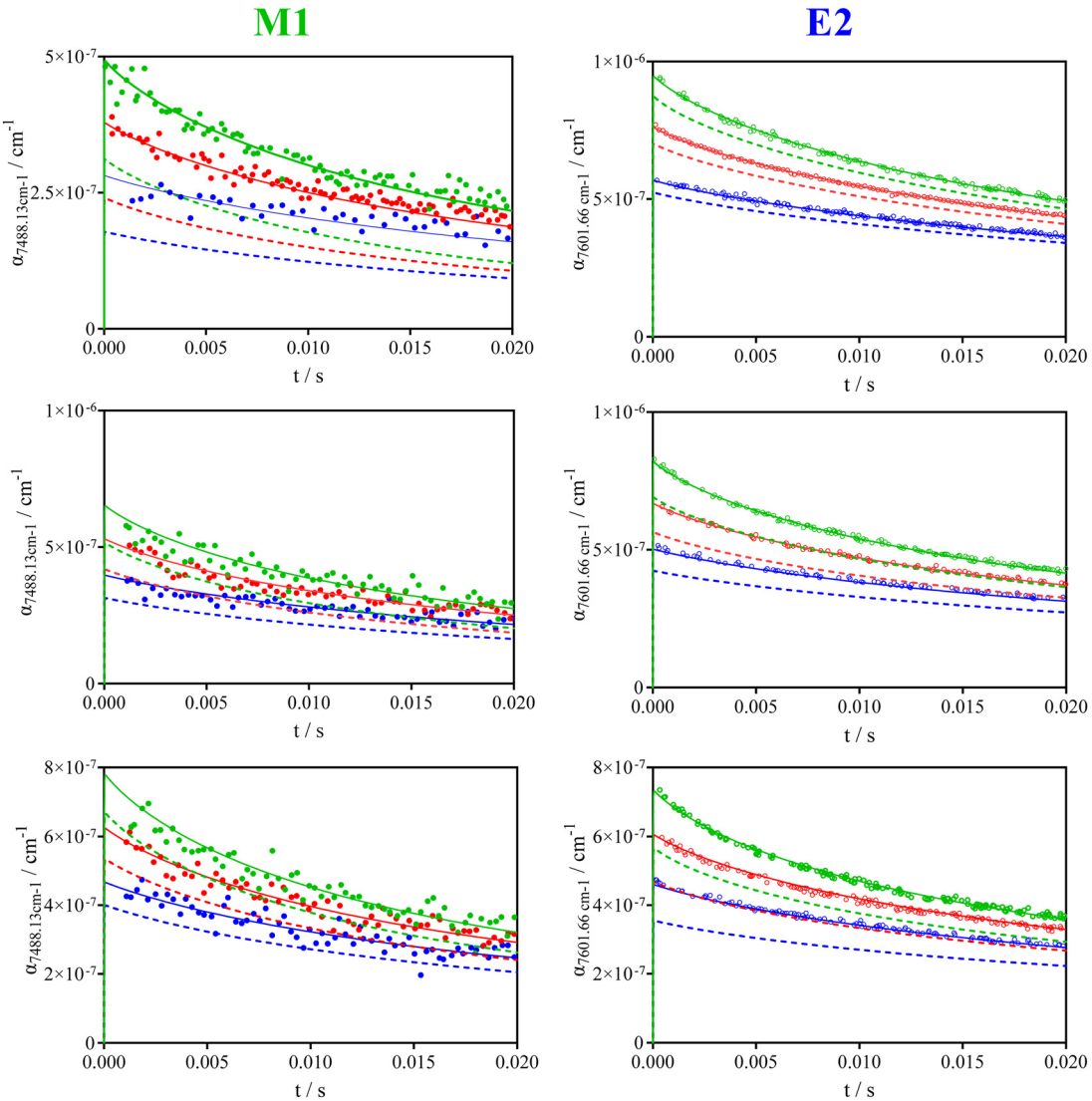

Fig. 2 Absorption-time profiles at M1 (left graphs) and E2 (right graphs) for all three series with conditions such as given in Table 2. Full lines present the simulated absorption-time profiles using the model from Table 3 and are presented as sum of absorbance due to CH_3O_2 and $C_2H_5O_2$, dotted lines represent the part of the absorbance due to major radical: CH_3O_2 in the left column, $C_2H_5O_2$ in the right column.

peroxy self-and cross reactions and the consumption through cross reaction of HO_2 with the peroxy radicals. Best results are obtained with a branching ratio towards the radical channel of ϕ_{1a} = 0.40, *i.e.* very similar to the branching fraction of the two self-reactions, ϕ_{12a} = 0.32 and ϕ_{13a} = 0.37 for $C_2H_5O_2$ and CH_3O_2, respectively. To demonstrate the influence of the cross reaction on the HO_2 profiles, the full black lines in the right graph represent for the highest radical concentration the simulation with the best rate constant and a branching ratio varied by ±0.2. It can be seen that such variation of the branching ratio makes the model clearly deviating from the experimental results and therefore we estimate the uncertainty of the branching fraction from the comparison between model and experiment to be better than ±0.2.

However, a major problem for estimating the branching ratio in these experiments is, that even for the self-reactions of the simplest peroxy radicals CH_3O_2 and $C_2H_5O_2$ there are still large uncertainty in rate constant and branching ratio. For CH_3O_2 the IUPAC recommendation[54] since many years was $k_{13} = 3.5 \times 10^{-14}$ cm^3 s^{-1} with a branching ratio of 0.37 for the radical channel. In a very recent work, Onel *et al.*[12] have re-determined the rate constant and found only $k_{13} = (2.0 \pm 0.9) \times 10^{-14}$ cm^3 s^{-1}, nearly 2 times slower, but they confirmed the radical yield as recommended by IUPAC. They convincingly argue that earlier experiments suffered from interferences of the fast reaction of Cl-atoms with CH_3O_2 and this would have increased the apparent rate constant. The rate constant for the self-reaction of $C_2H_5O_2$ radicals was also recommended by IUPAC for many years at $k_{12} = 7.6 \times 10^{-14}$ cm^3 s^{-1} with a radical yield of 0.63, based on the measurement of stable end products. Recently, Noell *et al.*[14] and Shamas *et al.*[24] obtained through direct radical measurements a much lower yield for the radical path and a

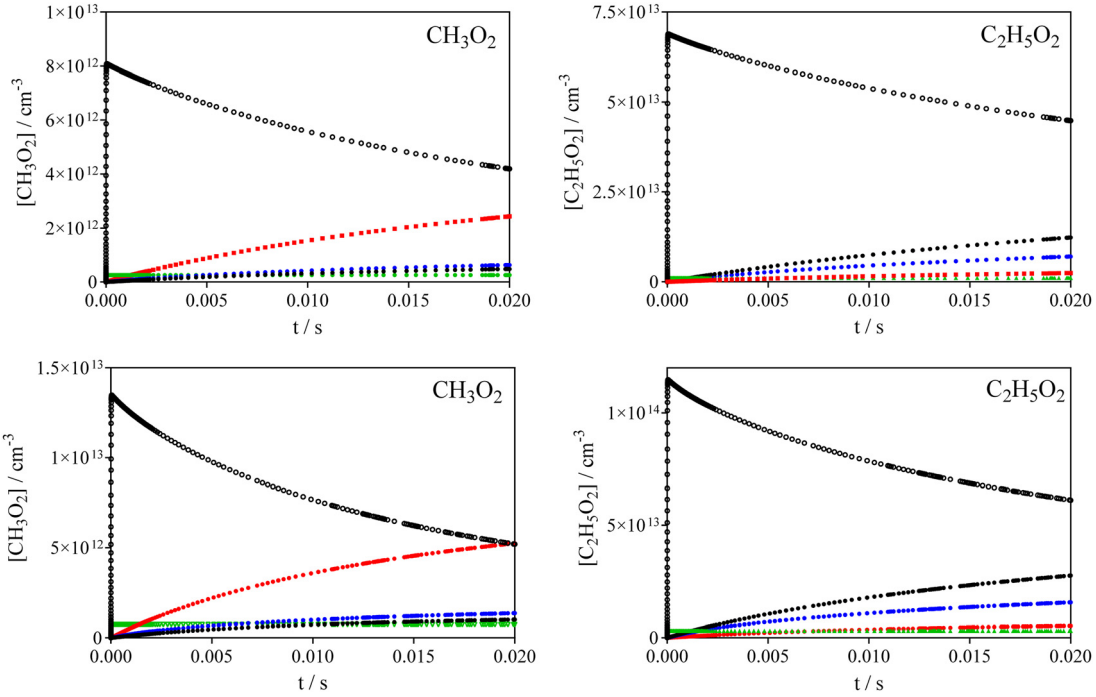

Fig. 3 Modeling results for conditions from first raw of Fig. 2 (highest excess of $C_2H_5O_2$). Left graph CH_3O_2, right graph $C_2H_5O_2$. Upper graphs are results for lowest Cl-concentration (blue symbols in Fig. 2), lower graph are results for highest Cl-concentration (green symbols in Fig. 2). Open black circles are $CH_3O_2/C_2H_5O_2$ concentration, blue symbols represent $CH_3O_2/C_2H_5O_2$ concentration having reacted through cross reaction with HO_2, black symbol represent $CH_3O_2/C_2H_5O_2$ concentration having reacted through self-reaction, green symbols represent $CH_3O_2/C_2H_5O_2$ concentration having reacted with Cl-atoms, red symbols represent $CH_3O_2/C_2H_5O_2$ concentration having reacted through cross reaction with $C_2H_5O_2/CH_3O_2$.

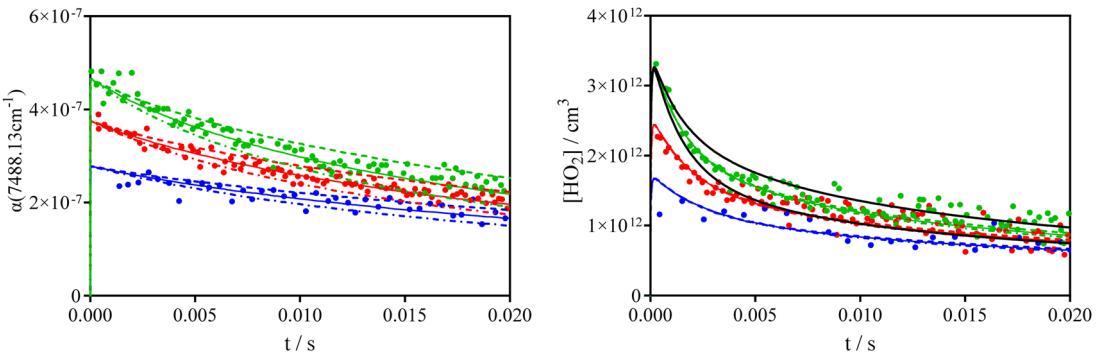

Fig. 4 Left graph: CH_3O_2 profiles for highest $C_2H_5O_2$ excess: full lines represent best simulation with rate constants from Table 3 (k_1 = 3.8 × 10^{-13} cm^3 s^{-1}), dashed lines represent a variation of k_1 of ±1.5 × 10^{-13} cm^3 s^{-1}. Right graph: HO_2 profiles for the same experiment. Full coloured line represents best model with a radical yield of 0.4, dashed lines in the right graph show the model with k_1 varied as shown in left graph, but the branching ratio varied to best reproduce experiment (see text). The black lines show a variation of ±0.2 for the branching ratio for the highest radical concentration.

subsequently higher rate constant (0.32 radical yield leading to k_{12} = (1.0 ± 0.2) × 10^{-13} cm^3 s^{-1}). A possible explanation for this disagreement could be a non-negligible yield of dimer-formation, ROOR, in the self-reaction of peroxy radicals. The decomposition of such dimer on reactor walls could lead to formation of aldehydes and thus appear as additional radical formation when measuring stable end products. The dimeric product has very recently been detected in the self-reaction of $C_2H_5O_2$[25] using advanced vacuum ultraviolet (VUV) photoionization mass spectrometry with a yield of 10 ± 5%. The dimer has also been directly detected by CIMS with a yield of 23% in the self-reaction of $HOC_2H_4O_2$ radicals and has been proven to decompose easily on quartz or metal surfaces.[67] But even though the cross reaction (R1) is the major HO_2 production path in the current experiments and the two self-reactions are only minor contributors, the above described uncertainties increase of course directly the uncertainty of the deduced yield in this work. Also, the HO_2 signal quality is poor in these experiments due to the absorption of high CH_4 and C_2H_6 concentrations, therefore we estimate the final uncertainty of the radical yield to be ϕ_{1a} = 0.40 ± 0.20. It should be noted that the uncertainty in the branching ratio has negligible influence on the determination

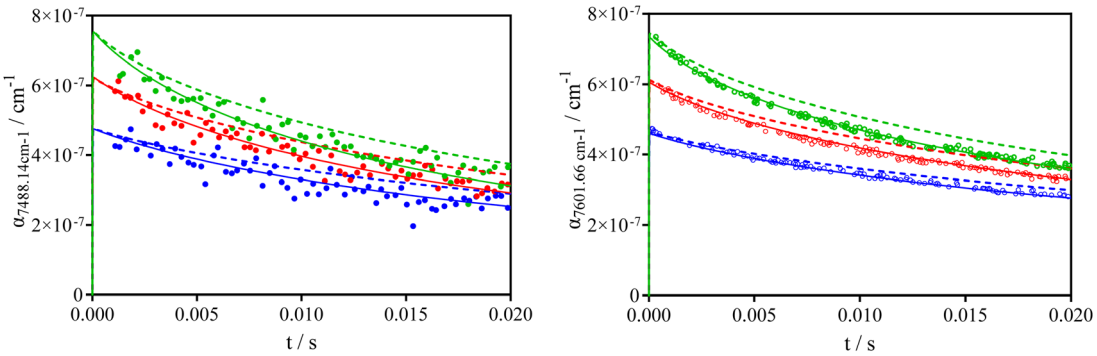

Fig. 5 Series of lowest $C_2H_5O_2/CH_3O_2$ ratio (lower raw in Fig. 3) with simulations using a rate constant for the cross reaction such as predicted by the geometric mean rule, if using data from Table 3 (full lines) and when using the recently determined rate constant for the CH_3O_2 self-reaction[12] (dashed lines).

of the rate constant: a change in radical yield for (R1) from 0.2 to 0.6 is barely visible in the modelled absorption-time profiles at both wavelengths.

To demonstrate the sensitivity of the observed absorption-time profiles to the rate constant of the cross reaction, the left graph of Fig. 4 shows the CH_3O_2 profiles of the same experiments, *i.e.* high excess of $C_2H_5O_2$. The full lines show again the model from Table 3, while the dashed lines represent a variation of $k_1 = (3.8 \pm 1.5) \times 10^{-13}$ cm^3 s^{-1}. Such variation brings the simulated profiles outside the experimental data. In these simulations, the branching ratio ϕ_{1a} has been adapted to best reproduce the HO_2 profiles (dashed coloured lines on the right graph): for the upper and lower limit of k_1, ϕ_{1a} was changed to 0.31 (for $k_1 = 4.8 \times 10^{-13}$ cm^3 s^{-1}) and 0.54 (for $k_1 = 2.8 \times 10^{-13}$ cm^3 s^{-1}) to best reproduce HO_2. However, this variation has no influence on the CH_3O_2 profiles as can be seen in Fig. 3 the cross reaction with HO_2 is only a minor path for CH_3O_2 and therefore a change in the branching ratio has a negligible effect on the CH_3O_2 profile. From these simulations we estimate the uncertainty of the rate constant of the cross reaction to be $k_1 = (3.8 \pm 1.0) \times 10^{-13}$ cm^3 s^{-1}.

The simulation corresponding to the lower limit of the rate constant (upper curves in Fig. 4) is close to the only published value for the cross reaction rate constant[45] ($k_1 = 2.0 \times 10^{-13}$ cm^3 s^{-1}), and is can be seen that the observed absorption time profiles are poorly reproduced by such a model. In the work of Villenave *et al.*[45] no details are given on how the rate constant was obtained by solely measuring UV absorption profiles, and therefore no speculation about possible reasons for the disagreement can be proposed.

The geometric mean value rule is an empirical approach that allows for the estimation of cross-reaction rate coefficients from the self-recombination rate constants of the reacting partners[68]

$$k_{A+B} = 2 \times \sqrt{k_{A+A} \times k_{B+B}}$$

It has shown to work to better than 20% in the prediction of radical–radical rate coefficients for a series of hydrocarbon radicals[69] and has proven to be valid also for the cross reaction of HO_2 and DO_2 radicals.[70] When applying this rule to the cross reaction of CH_3O_2 and $C_2H_5O_2$ and using the values for the self-reactions from Table 3, one obtains an excellent agreement ($k_{1,\text{geometric rule}} = 3.74 \times 10^{-13}$ cm^3 s^{-1}) with the rate constant obtained in this work. However, when using the value for the CH_3O_2 self-reaction recently obtained by Onel *et al.*,[12] the geometric mean rule predicts a rate constant for the cross reaction of only $k_1 = 2.9 \times 10^{-13}$ cm^3 s^{-1}. In Fig. 5 are shown the results for both wavelength for the experiments with the lowest $C_2H_5O_2$ excess, using this rate constant for the cross reaction.

It can be seen that this rate constant does not allow to reproduce the observed absorption-time profiles, as the decays at both wavelengths are clearly too slow. However, it has not been demonstrated that in the case of cross-reactions of peroxy radicals the geometric mean rule is a good approximation, in particular because there are no reliable determinations of the rate constants for self- and cross-reactions of peroxy radicals to validate the approach. Therefore, from the current experiments one cannot infer about the rate constant of the CH_3O_2 self-reaction. But it is clear that recent research using more selective detection methods for peroxy radicals, compared to UV absorption, have challenged long-standing results on even the simplest peroxy radicals, and more research is necessary to better understand their reactivity under low NO_x conditions.

Conclusion

The rate constant for the cross reaction of the two most simple and abundant peroxy radicals, CH_3O_2 and $C_2H_5O_2$, has been determined by following their concentration-time profiles in their respective Ã–X̃ electronic transition. A good selectivity has been obtained by working under excess of $C_2H_5O_2$ and by monitoring CH_3O_2 radical at 7488.13 cm^{-1} and $C_2H_5O_2$ radicals at 7602.25 cm^{-1}. A rate constant for the cross reaction of $k_1 = (3.8 \pm 1.0) \times 10^{-13}$ cm^3 s^{-1} and a yield for the radical channel of $\phi_{1a} = 0.40 \pm 0.20$ have been obtained. The present rate constant is nearly two times faster than the only earlier value, but in excellent agreement with an estimation based on the mean geometric rule. This work shows again, that the chemistry of peroxy radicals under low NO conditions is still

not well understood and more work is needed to improve the knowledge.

Conflicts of interest

There are no conflicts to declare.

Acknowledgements

This work is a contribution to the LabEx CaPPA project funded by the French National Research Agency under contract ANR-11-LABX-0005-01 and to the CPER research project ECRIN funded by the French Ministère de l'Enseignement Supérieur et de la Recherche. The authors thank the Regional Council ''Hauts-de-France'' and the ''European Regional Development Fund'' for their financial support to these projects. The authors thank Mohamed Assali and Mirna Shamas for assistance with initial experiments. C. Z. and C. L. thanks the Chinese Scholarship Council for financial support (no. 202006340125 (C. Z.) and no. 201908140178 (C. L.)). C. F. thanks the CAS for funding through PIFI no. 2018VMA0055.

References

1 J. J. Orlando and G. S. Tyndall, *Chem. Soc. Rev.*, 2012, **41**, 6294–6317.
2 G. S. Tyndall, R. A. Cox, C. Granier, R. Lesclaux, G. K. Moortgat, M. J. Pilling, A. R. Ravishankara and T. J. Wallington, *J. Geophys. Res.*, 2001, **106**, 12157–12182.
3 C. Fittschen, *Chem. Phys. Lett.*, 2019, **725**, 102–108.
4 B. Veyret, J. C. Rayez and R. Lesclaux, *J. Phys. Chem.*, 1982, **86**, 3424–3430.
5 R. A. Cox and G. S. Tyndall, *J. Chem. Soc., Faraday Trans.*, 1980, **76**, 153–163.
6 S. P. Sander and R. T. Watson, *J. Phys. Chem.*, 1981, **85**, 2960–2964.
7 K. McAdam, B. Veyret and R. Lesclaux, *Chem. Phys. Lett.*, 1987, **133**, 39–44.
8 M. J. Kurylo and T. J. Wallington, *Chem. Phys. Lett.*, 1987, **138**, 543–547.
9 M. E. Jenkin, R. A. Cox, G. D. Hayman and L. J. Whyte, *J. Chem. Soc., Faraday Trans.*, 1988, **84**, 913–930.
10 F. G. Simon, W. Schneider and G. K. Moortgat, *Int. J. Chem. Kinet.*, 1990, **22**, 791–812.
11 P. D. Lightfoot, R. Lesclaux and B. Veyret, *J. Phys. Chem.*, 1990, **94**, 700–707.
12 L. Onel, A. Brennan, F. F. Østerstrom, E. Cooke, L. Whalley, P. W. Seakins and D. E. Heard, *J. Phys. Chem. A*, 2022, **126**, 7639–7649.
13 F. C. Cattell, J. Cavanagh, R. A. Cox and M. E. Jenkin, *J. Chem. Soc., Faraday trans. II*, 1986, **82**, 1999–2018.
14 A. C. Noell, L. S. Alconcel, D. J. Robichaud, M. Okumura and S. P. Sander, *J. Phys. Chem. A*, 2010, **114**, 6983–6995.
15 H. Adachi, N. Basco and D. G. L. James, *Int. J. Chem. Kinet.*, 1979, **11**, 1211–1229.
16 C. Anastasi, D. J. Waddington and A. Woolley, *J. Chem. Soc., Faraday trans. I*, 1983, **79**, 505–516.
17 J. Munk, P. Pagsberg, E. Ratajczak and A. Sillesen, *J. Phys. Chem.*, 1986, **90**, 2752–2757.
18 T. J. Wallington, P. Dagaut and M. J. Kurylo, *J. Photochem. Photobiol., A*, 1988, **42**, 173–185.
19 D. Bauer, J. N. Crowley and G. K. Moortgat, *J. Photochem. Photobiol., A*, 1992, **65**, 329–344.
20 F. F. Fenter, V. Catoire, R. Lesclaux and P. D. Lightfoot, *J. Phys. Chem.*, 1993, **97**, 3530–3538.
21 D. B. Atkinson and J. W. Hudgens, *J. Phys. Chem. A*, 1997, **101**, 3901–3909.
22 H. Niki, P. D. Maker, C. M. Savage and L. P. Breitenbach, *J. Phys. Chem.*, 1982, **86**, 3825–3829.
23 T. J. Wallington, C. A. Gierczak, J. C. Ball and S. M. Japar, *Int. J. Chem. Kinet.*, 1989, **21**, 1077–1089.
24 M. Shamas, M. Assali, C. Zhang, X. Tang, W. Zhang, L. Pillier, C. Schoemaecker and C. Fittschen, *ACS Earth Space Chem.*, 2022, **6**, 181–188.
25 H. Yue, C. Zhang, X. Lin, Z. Wen, W. Zhang, S. Mostafa, P.-L. Luo, Z. Zhang, P. Hemberger, C. Fittschen and X. Tang, *Int. J. Mol. Sci.*, 2023, **24**, 3731.
26 Z. Wen, H. Yue, Y. Zhang, X. Lin, Z. Ma, W. Zhang, Z. Wang, C. Zhang, C. Fittschen and X. Tang, *Chem. Phys. Lett.*, 2022, **806**, 140034.
27 P. Dagaut, T. J. Wallington and M. J. Kurylo, *J. Phys. Chem.*, 1988, **92**, 3833–3836.
28 G. K. Moortgat, R. A. Cox, G. Schuster, J. P. Burrows and G. S. Tyndall, *J. Chem. Soc., Faraday Trans.*, 1989, **85**, 809–829.
29 P. D. Lightfoot, B. Veyret and R. Lesclaux, *J. Phys. Chem.*, 1990, **94**, 708–714.
30 A. A. Boyd, P.-M. Flaud, N. Daugey and R. Lesclaux, *J. Phys. Chem. A*, 2003, **107**, 818–821.
31 M. T. Raventós-Duran, M. McGillen, C. J. Percival, P. D. Hamer and D. E. Shallcross, *Int. J. Chem. Kinet.*, 2007, **39**, 571–579.
32 P. D. Lightfoot, P. Roussel, F. Caralp and R. Lesclaux, *J. Chem. Soc., Faraday Trans.*, 1991, **87**, 3213–3220.
33 P. Dagaut, T. J. Wallington and M. J. Kurylo, *J. Phys. Chem.*, 1988, **92**, 3836–3839.
34 M. M. Maricq and J. J. Szente, *J. Phys. Chem.*, 1994, **98**, 2078–2082.
35 M. T. Raventós-Duran, C. J. Percival, M. R. McGillen, P. D. Hamer and D. E. Shallcross, *Phys. Chem. Chem. Phys.*, 2007, **9**, 4338–4348.
36 A. Bossolasco, E. P. Faragó, C. Schoemaecker and C. Fittschen, *Chem. Phys. Lett.*, 2014, **593**, 7–13.
37 C. Fittschen, L. K. Whalley and D. E. Heard, *Environ. Sci. Technol.*, 2014, **118**, 7700–7701.
38 C. Yan, S. Kocevska and L. N. Krasnoperov, *J. Phys. Chem. A*, 2016, **120**, 6111–6121.
39 E. Assaf, B. Song, A. Tomas, C. Schoemaecker and C. Fittschen, *J. Phys. Chem. A*, 2016, **120**, 8923–8932.
40 C. Fittschen, M. Al Ajami, S. Batut, V. Ferracci, S. Archer-Nicholls, A. T. Archibald and C. Schoemaecker, *Atmos. Chem. Phys.*, 2019, **19**, 349–362.

41 R. L. Caravan, M. A. H. Khan, J. Zádor, L. Sheps, I. O. Antonov, B. Rotavera, K. Ramasesha, K. Au, M.-W. Chen, D. Rösch, D. L. Osborn, C. Fittschen, C. Schoemaecker, M. Duncianu, A. Grira, S. Dusanter, A. Tomas, C. J. Percival, D. E. Shallcross and C. A. Taatjes, *Nat. Commun.*, 2018, **9**, 4343.
42 E. P. Faragó, C. Schoemaecker, B. Viskolcz and C. Fittschen, *Chem. Phys. Lett.*, 2015, **619**, 196–200.
43 E. Assaf, C. Schoemaecker, L. Vereecken and C. Fittschen, *Int. J. Chem. Kinet.*, 2018, **50**, 670–680.
44 E. Assaf, S. Tanaka, Y. Kajii, C. Schoemaecker and C. Fittschen, *Chem. Phys. Lett.*, 2017, **684**, 245–249.
45 E. Villenave and R. Lesclaux, *J. Phys. Chem.*, 1996, **100**, 14372–14382.
46 J. Thiebaud and C. Fittschen, *Appl. Phys. B*, 2006, **85**, 383–389.
47 A. E. Parker, C. Jain, C. Schoemaecker, P. Szriftgiser, O. Votava and C. Fittschen, *Appl. Phys. B.*, 2011, **103**, 725–733.
48 O. Votava, M. Mašát, A. E. Parker, C. Jain and C. Fittschen, *Rev. Sci. Instrum.*, 2012, **83**, 043110.
49 E. Assaf, O. Asvany, O. Votava, S. Batut, C. Schoemaecker and C. Fittschen, *J. Quant. Spectrosc. Radiat. Transfer*, 2017, **201**, 161–170.
50 E. N. Sharp, P. Rupper and T. A. Miller, *Phys. Chem. Chem. Phys.*, 2008, **10**, 3955–3981.
51 E. P. Faragó, B. Viskolcz, C. Schoemaecker and C. Fittschen, *J. Phys. Chem. A*, 2013, **117**, 12802–12811.
52 C. Zhang, M. Shamas, M. Assali, X. Tang, W. Zhang, L. Pillier, C. Schoemaecker and C. Fittschen, *Photonics*, 2021, **8**, 296.
53 L. S. Rothman, I. E. Gordon, Y. Babikov, A. Barbe, D. Chris Benner, P. F. Bernath, M. Birk, L. Bizzocchi, V. Boudon, L. R. Brown, A. Campargue, K. Chance, E. A. Cohen, L. H. Coudert, V. M. Devi, B. J. Drouin, A. Fayt, J. M. Flaud, R. R. Gamache, J. J. Harrison, J. M. Hartmann, C. Hill, J. T. Hodges, D. Jacquemart, A. Jolly, J. Lamouroux, R. J. Le Roy, G. Li, D. A. Long, O. M. Lyulin, C. J. Mackie, S. T. Massie, S. Mikhailenko, H. S. P. Müller, O. V. Naumenko, A. V. Nikitin, J. Orphal, V. Perevalov, A. Perrin, E. R. Polovtseva, C. Richard, M. A. H. Smith, E. Starikova, K. Sung, S. Tashkun, J. Tennyson, G. C. Toon, V. G. Tyuterev and G. Wagner, *J. Quant. Spectrosc. Radiat. Transfer*, 2013, **130**, 4–50.
54 R. Atkinson, D. L. Baulch, R. A. Cox, J. N. Crowley, R. F. Hampson, R. G. Hynes, M. E. Jenkin, M. J. Rossi and J. Troe, *Atmos. Chem. Phys.*, 2006, **6**, 3625–4055.
55 R. X. Fernandes, K. Luther and J. Troe, *J. Phys. Chem. A*, 2006, **110**, 4442–4449.
56 R. X. Fernandes, K. Luther, G. Marowsky, M. P. Rissanen, R. Timonen and J. Troe, *J. Phys. Chem. A*, 2015, **119**, 7263–7269.
57 C. Fittschen, A. Frenzel, K. Imrik and P. Devolder, *Int. J. Chem. Kinet.*, 1999, **31**, 860–866.
58 E. Assaf, C. Schoemaecker, L. Vereecken and C. Fittschen, *Phys. Chem. Chem. Phys.*, 2018, **20**, 8707.
59 R. Atkinson, D. L. Baulch, R. A. Cox, J. N. Crowley, R. F. Hampson, R. G. Hynes, M. E. Jenkin, M. J. Rossi and J. Troe, *Atmos. Chem. Phys.*, 2004, **4**, 1461–1738.
60 V. Daele and G. Poulet, *J. de Chimie Physique*, 1996, **93**, 1081–1099.
61 R. Atkinson, D. L. Baulch, R. A. Cox, J. N. Crowley, R. F. Hampson, R. G. Hynes, M. E. Jenkin, M. J. Rossi, J. Troe and T. J. Wallington, *Atmos. Chem. Phys.*, 2008, **8**, 4141–4496.
62 R. Atkinson, D. L. Baulch, R. A. Cox, J. N. Crowley, R. F. Hampson, R. G. Hynes, M. E. Jenkin, M. J. Rossi and J. Troe, *Atmos. Chem. Phys. Discuss*, 2007, **7**, 981–1191.
63 E. Delbos, C. Fittschen, H. Hippler, N. Krasteva, M. Olzmann and B. Viskolcz, *J. Phys. Chem. A*, 2006, **110**, 3238–3245.
64 M. M. Maricq, J. J. Szente, E. W. Kaiser and J. Shi, *J. Phys. Chem.*, 1994, **98**, 2083–2089.
65 E. P. Clifford, J. T. Farrell, J. D. DeSain and C. A. Taatjes, *J. Phys. Chem. A*, 2000, **104**, 11549–11560.
66 J. D. DeSain, S. J. Klippenstein, J. A. Miller and C. A. Taatjes, *J. Phys. Chem. A*, 2003, **107**, 4415–4427.
67 S. E. Murphy, J. D. Crounse, K. H. Møller, S. P. Rezgui, N. J. Hafeman, J. Park, H. G. Kjaergaard, B. M. Stoltz and P. O. Wennberg, *Environ. Sci.: Atmos.*, 2023, **3**, 882–893.
68 A. W. Jasper, S. J. Klippenstein and L. B. Harding, *J. Phys. Chem. A*, 2007, **111**, 8699–8707.
69 S. J. Klippenstein, Y. Georgievskii and L. B. Harding, *Phys. Chem. Chem. Phys.*, 2006, **8**, 1133–1147.
70 M. Assali, J. Rakovsky, O. Votava and C. Fittschen, *Int. J. Chem. Kinet.*, 2020, **52**, 197–206.